Article

The Role of Pulse Duty Cycle and Frequency on Dendritic Compression

Published as part of The Journal of Physical Chemistry virtual special issue "Michael R. Hoffmann Festschrift".

Trina Dhara,[∇] Asghar Aryanfar,* Asmita Ghosh, Udita Ghosh, Partha Mukherjee, and Sunando DasGupta*

Read Online

| ACCESS | Metrics & More | Article Recommendations | SI Supporting Information |

ABSTRACT: The formation of dendritic microstructures during the charging period of the battery is a critical phenomenon, hampering the sustainable utilization of energy-dense materials, such as alkaline metals as the electrode. We establish a new experimental setup and measure for tracking the dendritic tendency in real time to quantify the dendritic compression versus the conventional parameters of pulse duty cycle and frequency. In this regard, we close the scale gap between experiments (∼mm, ∼s) and affordable simulations (∼nm, ∼ms) by means of coarse-grained modeling. Analyzing the nonlinear variation of the investigated parameters versus the pulse and rest periods, we explain the limits where they remain effective, based on the formation/relaxation of the respective layers. The obtained results can be useful for designing the dendrite-resilient pulse parameters via the simultaneous utilization of experiments and simulations.
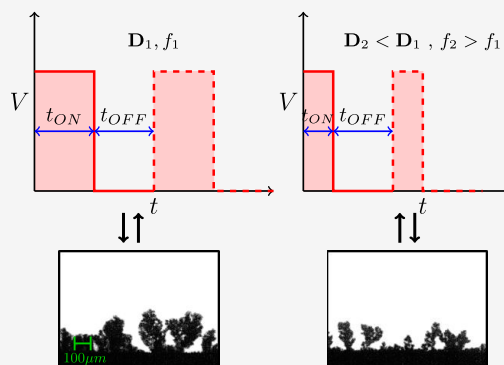
1. INTRODUCTION

Over the past decade, rechargeable lithium-based batteries have been extensively studied to be utilized as a means of energy storage for diverse electronic devices.[1,2] Particularly, the prolonged cycle lives, high power density, and safe performance are demanded in a large number of emerging applications, such electric vehicles.[3,4] However, the limited energy storage capacity of those batteries has been the major barrier toward application in heavy duty operations.[5] The conventional lithium ion batteries (LIBs), consisting of transition-metal oxide cathodes paired with graphite anodes[6] which lacks sufficient specific capacity (372 mA h g^{-1})[7] to meet the ever-increasing energy and computational demand.[8,9] The commonly proposed candidate for replacement is the lithium metal anode (Li^0), because of its extreme theoretical high specific capacity (3860 mA h g^{-1})[10,11] coupled with very low negative electrochemical potential (−3.04 V vs standard hydrogen electrode (SHE)). However, the associated issue with their application lies in the random and uncontrolled growth of the dendritic branches, which may cause catastrophic damage to the electrolytic cell. The growing microstructure could penetrate the separator, bridge the electrodes, and cause a short circuit. On separate occasions, the dendritic branch may get broken down from a thin neck, and get shielded completely by the insulating solid electrolyte interface (SEI) from the electrode,[12] forming dead lithium crystals as a lost active material.[13,14] Such disconnection causes the columbic

deprivation and reduction in the state of health (SOH). Additionally, the dead lithium can increase the resistance for the incoming charge carrier and trigger the thermal runaway, because of their extreme surface-to-area ratio.[15]

Nonetheless, this issue is not limited to lithium metal (Li) only and has been observed for other metal candidates such as magnesium (Mg),[16] sodium (Na),[17,18] aluminum (Al),[19] and zinc (Zn),[20] and significant efforts have been ongoing with regard to the structural control/suppression of their unrestrained microstructures during the charging period.[21]

Experiment-wise, several factors can alter the morphology of the electrodeposits, such as current density,[22,23] electrolyte composition,[24,25] roughness of the electrode surface,[26,27] additives,[28] and temperature.[29,30] For LIBs, the addition of metal cations with a smaller reduction potential value, compared to Li$^+$ ions, such as Cs$^+$ and Rb$^+$, are likely to form an electrostatic shield over the high-energy spots on the electrode surface.[31] Similarly, several recent studies have designed separator structures,[32,33] structured electrolyte,[34]
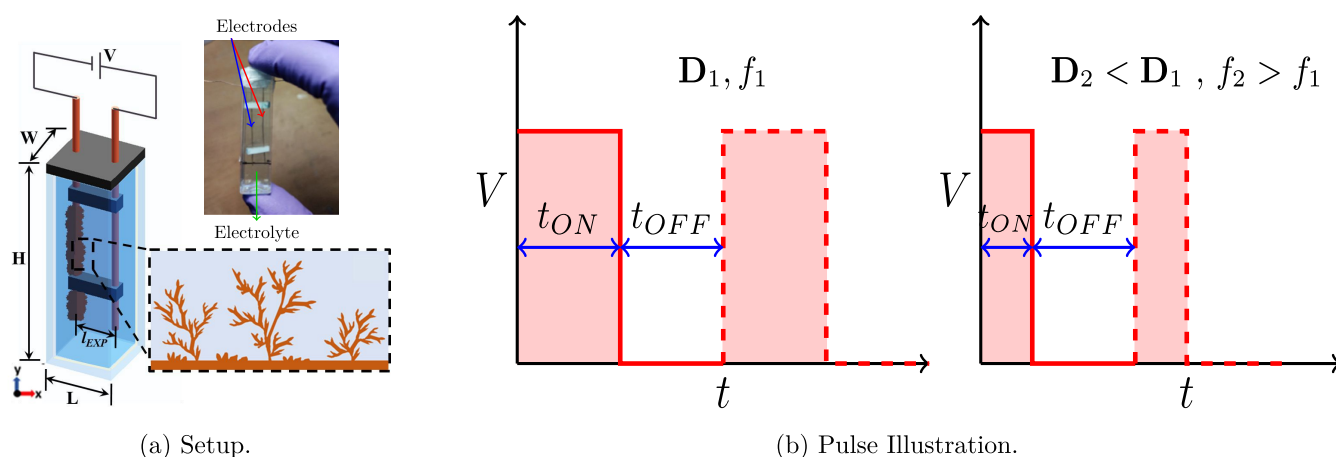
Figure 1. (a) Experimental setup and (b) charging characterization.

and electrode material,[35] gel polymer electrolyte,[36] and three-dimensional (3D) porous current collectors.[37,38]

Modeling-wise, earlier frameworks focused on space charge region and the strength of the electric field as the governing factors behind the dendritic growth.[39] Later on, the effect of the ionic concentration was adopted as the main responsible drive for their evolution during the diffusion limited aggregation (DLA)[40−44], and the respective root-cause and mechanism was analyzed for the formation tree-like structures.[45]

Among the proposed methods to suppress the dendritic evolution, the regulation of charging strategy has been proven to be promising, since this method does not involve the alteration of internal components of the battery such as electrolyte, electrode, and surface roughness, etc. Instead, it utilizes external modulation of applied potential difference (V)/current density (i), in terms of prescribed pulsation, which has been shown in earlier simplistic models.[46]

For instance, a complete prevention of dendritic growth and significant reduction in surface roughness has been reported for zinc (Zn) electrodeposition via applying pulse trains,[47] where, since the current density correlates directly with nucleation, a high amplitude nucleation pulse has been followed by the series of low amplitude pulse trains. In addition, the cycle life[48] and efficiency[49] of the LIB have been improved, compared to DC charging. Similar high-to-low voltage train has been proven as efficient dendrite resilient charging protocol in the recent simulations.[50] Furthermore, the higher efficacy of pulse-reverse charging has been related to the melting of the dendritic tips and flattening the growing interface during the partial-reverse charge period.[51] It is even more interesting to recall that the duration and ratio of the intermittent pause t_{OFF} (i.e., when the interelectrode potential turns zero) and pulse t_{ON} (i.e., duration of applied pulse for electrodeposition) periods plays a very important role in the ramification amount of the growing electrodeposits. It has been shown that the decreasing t_{ON} can compress the dendrites up to ~2.5 times, compared to uniform charging.[52] In addition, a real-time feedback control framework has been established to minimize branched microstructure based on the instantaneous relaxation time, as a function of the radius of curvature in the accelerating tips.[53] Such curvature-dependent concentration profile is periodically established and relaxed in the electro-deposition interface.[54] However, the real-time evolution of electrode−electrolyte interfacial undulations during pulse t_{ON}

and pause t_{OFF} durations, particularly in terms of conventional duty cycles and frequency ranges, are scant in the literature.

The remaining question regarding the pulse-charging is that to what extent can the t_{ON} and t_{OFF} values be useful for efficient shortening of the growing dendrites. In this regard, the simpler expressions of duty cycle **D** and the pulse frequency f are the most tangible representative of both aforementioned parameters. Therefore, we have performed both experiments and simulations for studying their efficacy limits, by probing the interfacial tortuosity. We have performed both real-time image processing in the experiments and coarse-grained simulations for quantitative understanding and we have analyzed the underlying reasons based on the displacement factors during the pulse t_{ON} and rest t_{OFF} periods.

2. EXPERIMENTAL SECTION

2.1. Setup. In order to replicate the electrodeposition in batteries, we have fabricated a laboratory-made electrochemical cell, composed of symmetric copper wire electrodes,[55] because of their nontoxicity and environmental friendliness. The experimental setup shown in Figure 1a consists of a transparent plastic cuvette (4.5 cm × 1 cm × 1 cm) that functions as an electrolytic cell. The two wire electrodes (ARTIFACT, 99.9% purity, d = 0.27 mm) are inserted and dipped into analytical-grade copper sulfate pentahydrate (CuSO$_4$·5H$_2$O, EMPLURA, 99% purity) electrolyte solution of {0.025, 0.05} M concentration. More details of the experimental setup are available in the previous publication.[55] After each experiment, the cuvette is cleaned with isopropyl alcohol (IPA), followed by deionized water (DI, Milli-Q, 99.8%), and rinsed with the electrolyte solution to be used for performing the next experiment. The copper wires are cleaned with acetone and ethanol to remove any oily residue present on the surface. The wires are inserted through the two insulating pieces of separators, made of synthetic rubber, to maintain the constant interelectrode gap (L) inside the cuvette. Thereafter, the entire cuvette is filled up to the brim with the electrolyte solution to ensure the absence of any internal bubbles. Consequently, the cell is sealed with Parafilm over the lid to avoid any leakage of the solution.

The cuvette is placed in line with a camera and the evolution of the dendrites is captured by using an image acquisition camera system at the rate of 183 frames per second (fps)). This ensured that, in each experiment, the optical parameters such as brightness, contrast, saturation, and gain remain constant to maintain equivalent analogy on the taken images.

The imposed charging was performed via pulse trains illustrated in Figure 1b containing intermittent rest periods with the intervals of t_{ON} and t_{OFF}, respectively. The pulse frequency f was defined as the inverse of the total pulse−rest cycle time as

$$f = \frac{1}{t_{ON} + t_{OFF}} \quad (1)$$

Additionally, the duty cycle ($\mathbf{D}$) was defined as the fraction of the total cycle period that the pulse is active; hence,

$$\mathbf{D} = \frac{t_{ON}}{t_{ON} + t_{OFF}} \quad (2)$$

Multiple square pulse waves were applied under a voltage of 6 V for the frequencies of $f = \{1, 10, 100, 1000\}$ Hz and duty cycle values of $\mathbf{D} = \{1/2, 1/3, 1/4, 1/6\}$, which was produced by an arbitrary waveform generator (SIGLENT, Model SDG6022X). Additionally, before performing each set of experiments, the output voltage of the waveform generator was validated with the oscilloscope (SIGLENT, Model SDS 1202X-E). Each experiment, with the parameters shown in Table 1, was performed at least three times to ensure the

Table 1. Experimental Parameters

parameter	value	unit
l_{EXP}	0.5	cm
d	0.27	mm
V	6	V
f	{1, 10, 100, 1000}	Hz
$\mathbf{D}$	{1/2, 1/3, 1/4, 1/6}	−
C	{0.025, 0.05}	M

consistency. The real-time images were captured and the frames were extracted from the captured videos in MATLAB and further processed for image analysis.

2.2. Characterization of the Electrodeposits. The captured images were binarized and analyzed in an open software, ImageJ, to evaluate the fraction of deposited area f_{DEP} with the average $\overline{y}$ and maximum y_{max} heights of the electrodeposits.[56] The binarization has been performed via the Otsu's method,[57] where the RGB image is inserted into the program with the three color values of $\{R, G, B\} \in [0, 255]$ and has been extracted and normalized to a grayscale intensity image I with individual values of range $I_{i,j} \in [0, 1]$. Subsequently, the grayscale image $I_{i,j}$ is binarized into $J_{i,j}$ via the grayness threshold I_c, such that

$$J_{i,j} = \begin{cases} 1 & I_{i,j} \geq I_c \\ 0 & I_{i,j} < I_c \end{cases}$$

The threshold value I_c has been chosen to minimize the weighted intraclass variance σ^2 defined proportionally as

$$\begin{cases} \sigma^2 = \omega_0 \sigma_0^2 + \omega_1 \sigma_1^2 \\ \omega_0 + \omega_1 = 1 \end{cases}$$

where ω_0 and ω_1 are the individual weight of each portion as the fraction of total, divided by the value of I_c and σ_0^2 and σ_1^2 are their respective variances.[57] Such minimization ensures that the resulted binary medium of black and white pixels

individually fall to the closest proximity of each other, when counted in the same group (i.e., closest ≈ lowest variance).

Second, the average height of the electrodeposits $\overline{y}$ is the extent of deposition height evaluated by scaling the black area to the horizontal frame length and calibrated to the physical value in micrometers (μm). Figure 2 schematically shows the
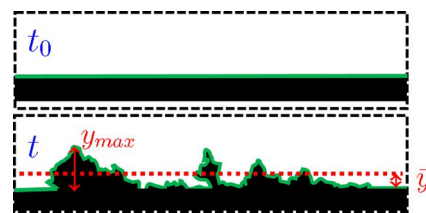

Figure 2. Illustration of the average $\overline{y}$ and maximum y_{max} heights and their transient evolution. The green line is used for the tortuosity τ measurements.

such average value as well as the maximum height y_{max}. We quantify the dendritic propensity by calculating the tortuosity (τ) of the transient interfacial length $l(t)$ as

$$\tau = \frac{l(t)}{l_0} \quad (3)$$

where l_0 is the original length of the interface (i.e., width). The last image from each experiments are shown versus the frequency f and duty cycle $\mathbf{D}$ is shown in Figures 3 and 4, respectively. Respective movies of growth are provided in the Supporting Information.
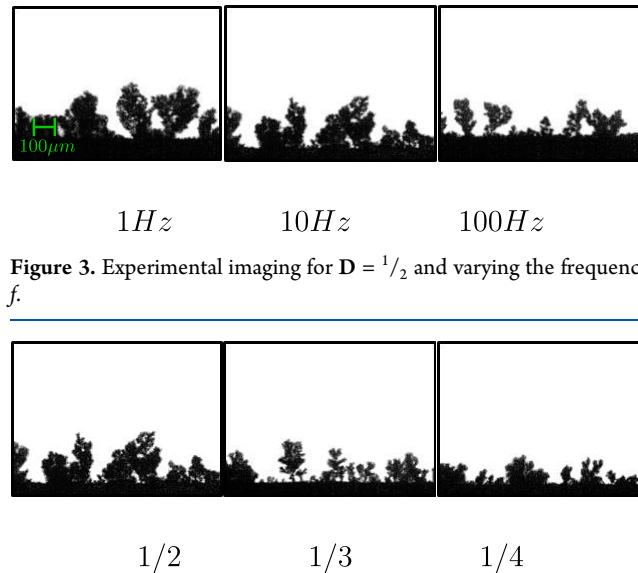

$$1Hz \qquad 10Hz \qquad 100Hz$$

Figure 3. Experimental imaging for $\mathbf{D} = {}^1\!/_2$ and varying the frequency f.
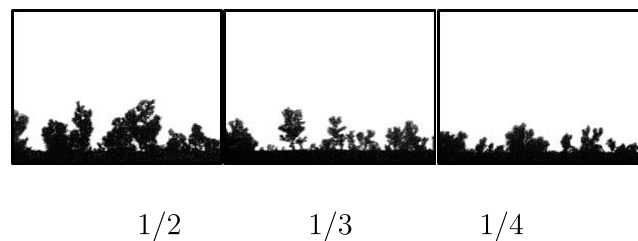

$$1/2 \qquad 1/3 \qquad 1/4$$

Figure 4. Experimental imaging for $f = 10$ Hz, and varying duty cycle $\mathbf{D}$.

Consequently, to get more insights of the depositing structures, the sample electrodes were taken out and carried into the electron microscope for analysis via field-emission scanning electron microscopy (FESEM) (JEOL, Model JSM-7610F) where the SEM images were acquired versus the change in frequency and duty cycle, as shown in Figures 5a and 5b. In this regard, note that the dendritic structures are brittle in nature. Therefore, the electrolyte solution is syringed out from the cuvette very slowly after the experiments, and then
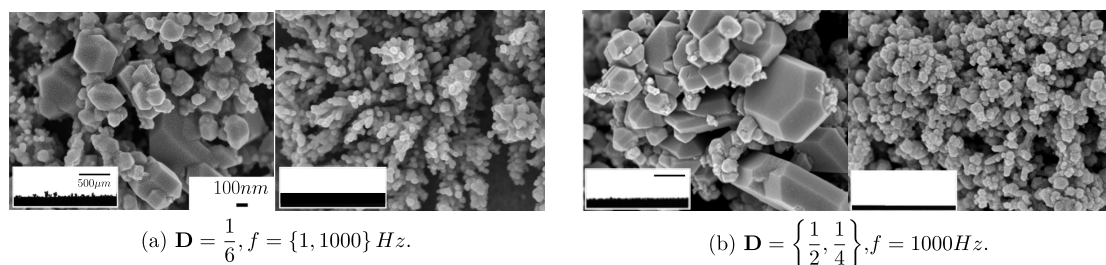
(a) $\mathbf{D} = \frac{1}{6}, f = \{1, 1000\}\, Hz.$ (b) $\mathbf{D} = \left\{\frac{1}{2}, \frac{1}{4}\right\}, f = 1000 Hz.$

Figure 5. SEM image comparison of the samples versus (a) frequency f and (b) duty cycle $\mathbf{D}$. Insets show the larger-scale morphologies (scale bars are the same for all images).
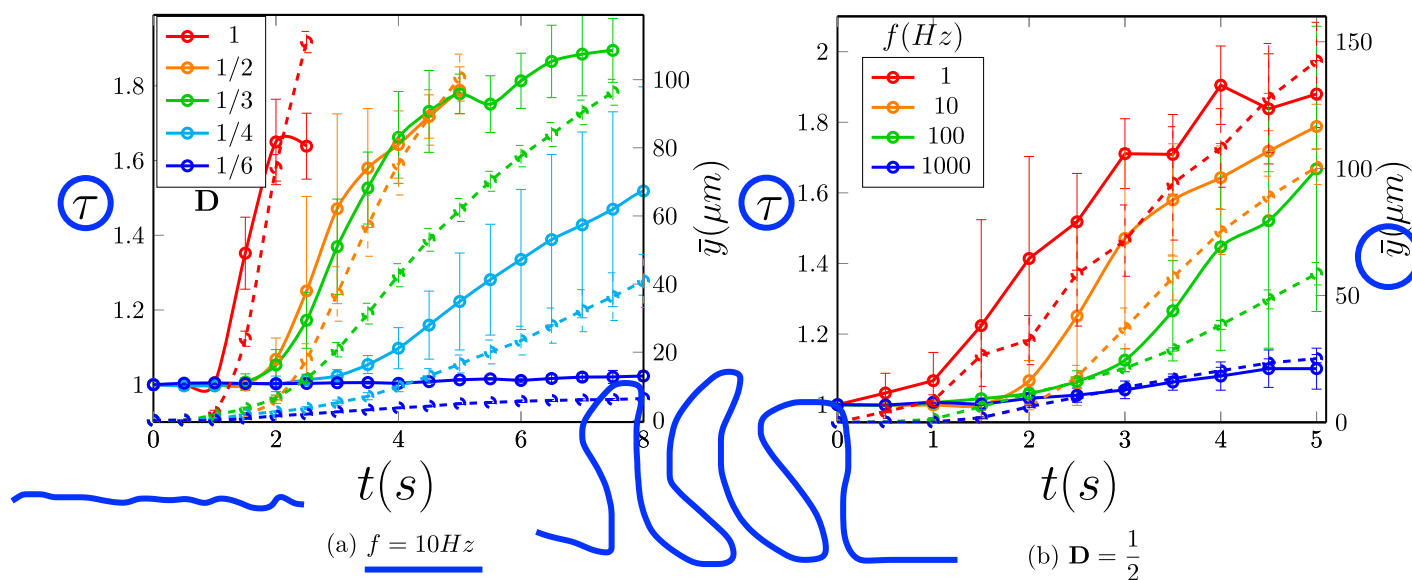

(a) $f = 10 Hz$ (b) $\mathbf{D} = \frac{1}{2}$

Figure 6. Transient growth in tortuosity τ as the dendritic measure and their respective average height $\overline{y}$ versus duty cycle (a) and frequency (b). (a) The dendritic interface is considerably flattened versus the reducing the pulse duty cycle, and their height is reduced by $\sim$25% in the investigated range. The curve of $\mathbf{D} = 1$ corresponds to DC charging. (b) The dendrites are significantly compressed versus increasing the pulse frequency f by as much as 40%. In all cases the total charging time is maintained constant for equivalency where $\sum t_{ON} = 2.5$ s (the figure is cropped at 8 s to show detailed visualization).

the electrodes are taken out. The samples are kept under vacuum until placed inside the SEM chamber for imaging.

Since t_{ON} correlates with the reaction time, for lower duty cycles $\mathbf{D}$, the experiment is extended, such that the cumulative reaction time remained constant $\sum t_{ON} = 2.5$ s. The transient evolution of the tortuosity τ as well as the average height $\overline{y}$ is illustrated versus the applied frequency f and duty cycle $\mathbf{D}$ in Figures 6a and 6b, respectively.

3. SIMULATION FRAMEWORK

We have adopted the coarse grained modeling in time and space, which works based on the averaging estimation for the progress of the diffusive wave during prolonged interionic random walks. In the electrochemical system, the coarse-scale displacement of an ion is the combinatoric effect of the two distinct movements of diffusion and electromigration. Regarding the former, the ions have a tendency to collide with each other and repel each other during the interionic collisions and, given the coarse time interval δt, their displacement $\delta \mathbf{r_D}$ wouldbe

$$\delta \mathbf{r_D} = \sqrt{2D\delta t}\,\hat{\mathbf{g}}$$

where D is the diffusivity of the ions in the electrolytic solution and $\hat{\mathbf{g}}$ is a random unit vector, representing the Brownian

motion. In fact, the value $\sqrt{2D\delta t}$ illustrates the mean square displacement of the diffusive wave, attained directly by solving the classical diffusion equation.[58]

Regarding the latter, the charge carriers are exposed to an external electric field $\mathbf{E}$, initially accelerate, and quickly reach a constant drift velocity of $\mu \mathbf{E}$. Hence, their electromigration displacement $\delta \mathbf{r_M}$ in the given time interval δt is obtained as

$$\delta \mathbf{r}_M = \mu \mathbf{E}\delta t$$

Therefore, the total ionic displacement $\delta \mathbf{r}$ is the sum of the aforementioned factors as

$$\delta \mathbf{r} = \delta \mathbf{r}_D + \delta \mathbf{r}_M$$

which is visualized in Figure 7. Regarding the electric field, the potential distribution was obtained by solving the Laplace equation using the finite difference method,[52] in real time. The electroneutrality was assumed for computing the electric field and, hence, the instantaneous potential distribution by imposing the growing boundary condition is due to change in the geometry of the interface.

To start the simulation, a random distribution of ions in the space was assumed. Subsequently, in every time increment δt, the corresponding displacement of the ions from diffusion ($\delta \mathbf{r}_D$) and electromigration ($\delta \mathbf{r}_M$) were calculated, resulting in
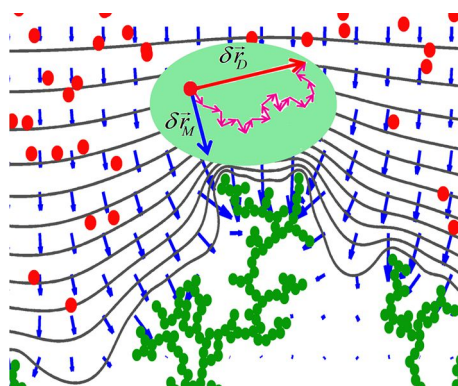
Figure 7. Coarse-grained framework, showing the displacement elements involved. [Legend: red vector, diffusion; blue vector, electromigration; pink vector, smaller displacement due to interionic collisions; red circles, free ions; green branches, dendrites; gray lines, isopotential contours). Reprinted with permission from ref 54. Copyright 2019, American Physical Society.]

a total displacement $\delta\mathbf{r}$. Periodic boundary conditions were applied in the x-direction; for example, every ion exiting the domain boundaries automatically enters the domain from the opposite side ($x + l_{SIM}$ for exiting from the left and $x - l_{SIM}$ for exiting from the right). Similarly, for the y-direction, if an ion leaves from above the domain, that move is canceled and another ion is added to the same y-position at a random x. When the moving ions either reach the bottom surface or overlap with the already-established dendrite structure, they turn into the dendrite and another free ion is added from the top interface to keep the ionic flow steady and the number of the present free ions constant. The attachment condition could be mathematically expressed as

$$|\mathbf{r}_{SEP,i} - \mathbf{r}_{DND,j}| \leq d_{Bond}$$

where $\mathbf{r}_{SEP,i}$ and $\mathbf{r}_{DND,j}$ are the position vectors of a random moving ion and a random stationary dendrite atom, and d_{Bond} is the bond distance ($d_{Bond} = 2.56 \times 10^{-10}$ m).[59] In this regard, the probability p of bonding upon overlap is considered to be unity, which means that the ion turns into a dendrite immediately upon getting close enough to the dendritic structure. The simulation is stopped when the number of atoms in the dendrite reaches the prescribed value of $N = 600$, which excludes the initial flat atoms describing the electrode surface. The dendritic interface was assumed to be a distance of $1.3r_{Bond}$ from the interfacial atoms, which is a very close contour to the dendrite. Subsequently, it was tracked and measured for interface tortuosity τ, based on eq 3.

In order to establish an analogous comparison between the experiments and simulations, one must develop an affordable

simulation framework that contains the key parameters describing the experimental electrochemical system and the method of electrodeposition. In this regard, we focus on the characteristic parameters presented in Table 2.

3.1. Transition Time. The transition (i.e., characteristic) time is a time measure for the diffusion of the ions in an electrochemical cell. The pulse-charging contains trains of both charge period with Faradaic reactions, followed by the rest period for charge concentration relaxation, both of which merely occur in the double-layer region with the estimated scale of Debye length (λ_D) as described below:

$$\lambda_D = \sqrt{\frac{\varepsilon\varepsilon_0 RT}{ez^2 FC_0}} \tag{4}$$

where ε is the relative permittivity of the electrolytic medium, ε_0 the vacuum permittivity, R the universal gas constant, T the absolute temperature, e the electron charge, z the valency of the ion, F the faradaic constant, and C_0 the bulk concentration.

Therefore, for a large-scale experimental observation performed in the domain l_{EXP}, an appropriate characteristic time t_{EXP} could be measured from their geometric mean as[60]

$$t_{exp} \approx \frac{\lambda_D l_{EXP}}{D_{EXP}}$$

which pertain to both local (i.e., λ_D) and global (i.e., l_{EXP}) effects.

On the other hand, the scale of atomistic simulations is typically given in nanometers ($l_{SIM} \approx$ nm) while the Debye length is typically given in micrometers ($\lambda_D \approx \mu$m). Hence, since the atomistic events occur in far smaller scale ($l_{SIM} \ll \lambda_D$), the appropriate length scale for the formation of charge density and its relaxation during the pulse charging would occur in a much smaller domain (l_{SIM}) per se, and the respective characteristic simulation time t_{SIM} could be defined solely by means of local relaxation as

$$t_{SIM} \approx \frac{l_{SIM}^2}{D_{SIM}}$$

Hence, in order to pertain to equivalent concentration relaxation times, we scale the diffusivity value D by equating the transition time scales between the experiments t_{EXP} and simulations t_{SIM} ($t_{SIM} = t_{EXP}$) where the reduced diffusivity D_{SIM} for the simulations is defined as follows:

$$D_{SIM} = \alpha D_{EXP} \tag{5}$$

where α is the coefficient of reduction for the diffusivity ($\alpha = l_{SIM}^2/\lambda_D l_{EXP}$), to attain affordable computation. The value of D_{SIM} is given in the values presented in Table 2. In addition, the reduction of the diffusivity to D_{SIM} makes

Table 2. Simulation Parameters

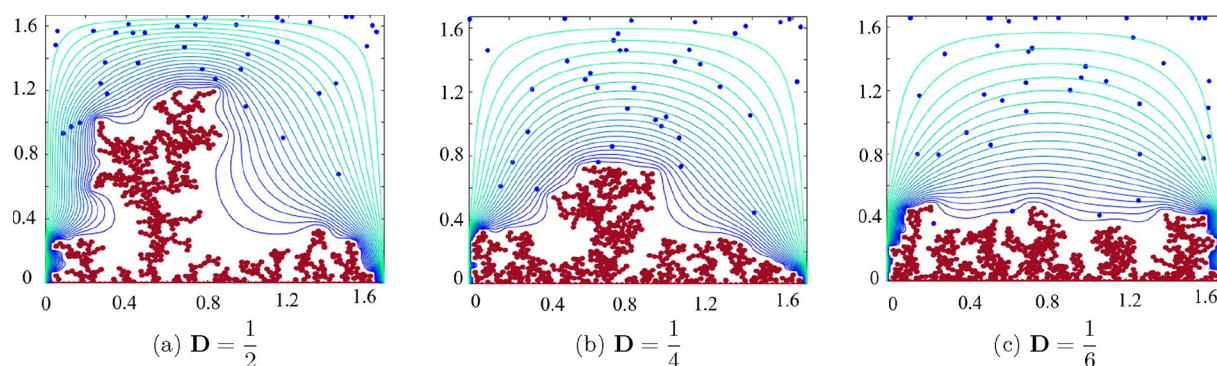| parameter	value	unit	source	experimental parameter	value	unit
$D(0.05$ M$)$	4.4×10^{-10}	m^2 s^{-1}	ref 61	f	{10, 100, 1000}	Hz
D_{SIM}	3.62×10^{-14}	m^2 s^{-1}	eq 5	$\mathbf{D}$	{12, 14, 16}	–
V	~50	mV	eq 8	δt	1	μs
ε_0	8.82×10^{-12}	F m^{-1}	ref 62	T	298	K
ε	85	–	ref 63	z	2	–
R	8.314	J mol^{-1} K^{-1}	ref 62	C_0	0.5	M
F	96.5	kC mol^{-1}	ref 64	l_{SIM}	16.7	nm
e	1.6×10^{-19}	C	ref 64	N	600	[ ]

Figure 8. Simulation morphologies obtained versus varying the duty cycles **D** of (a) $^1/_2$, (b) $^1/_4$, and (c) $^1/_6$. [Legend: red, dendrites; blue, free ions; lines, isopotential contours (dimensions given in terms of $\times 10^{-8}$ m). $f = 1000$ Hz, $N = 600$.]
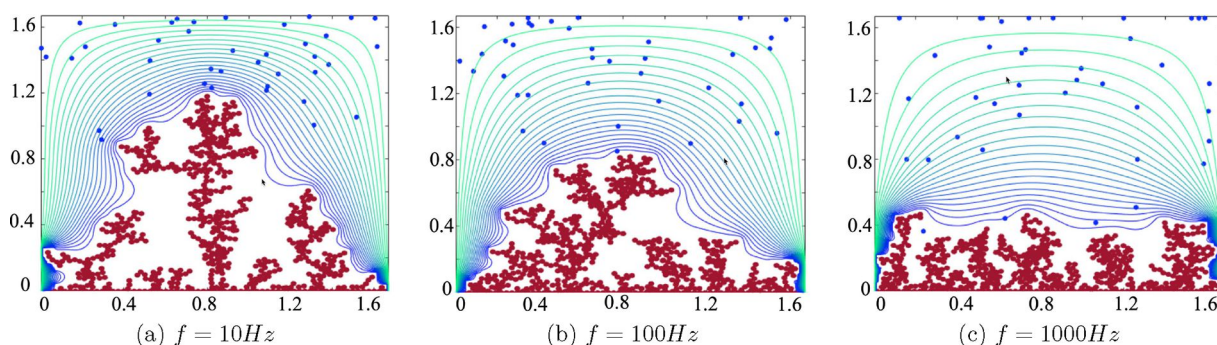

Figure 9. Simulation morphologies obtained versus varying the frequency f of (a) 10 Hz, (b) 100 Hz, and (c) 1000 Hz. (dimensions are given in terms of $\times 10^{-8}$ m). **D** = $\frac{1}{6}$, $N = 600$.]

significantly fewer atoms leae the boundary, leading to more realistic results with regard to dendrite formation.

3.2. Pulse Efficacy. Typically for an effective pulse charging, the two terms of $\delta\mathbf{r}_M$ and $\delta\mathbf{r}_D$ must competitive, so the relaxation during the pause period could avoid the buildup during the pulse. Henceforth, the other important factor for the efficacy of the pulse charging is the competitiveness of the displacements in the pulse period t_{ON} with the rest period t_{OFF}. Equating the respective displacements (MSD $\approx$ EMD), we get

$$\sqrt{2D_{SIM}\delta t} \approx \frac{D_{SIM}e}{k_B T}E_{ave}\delta t \qquad (6)$$

where e is the electron charge, k_B the Boltzmann constant, T the absolute temperature, and E_{ave} the average electric field in the equivalent simulation medium, which can be obtained from the expression $E_{ave} = V/d$. Since the range of d varies and, in fact, covers the entire medium $0 < d < l_{SIM}$, the range of electric field will be $V/l_{SIM} < E < \infty$. Herein, we choose the candidate value of MSD in this range as an approximation; hence,

$$E_{ave} \approx \frac{V_{SIM}}{\sqrt{2D_{SIM}\delta t}} \qquad (7)$$

Combining eqs 6 and 7, we get a measure for the voltage scale V_{SIM} in the equivalent simulation medium as

$$V_{SIM} = \frac{2k_B T}{e} \qquad (8)$$

For simulations, the position of the Cu ions is randomly initialized at $t = 0$. The ions were allowed to perform random

walks during simulation time increments δt of the pulse charging as follows:

$$\begin{cases} t_{ON} & \text{MSD + EMD} \\ t_{OFF} & \text{MSD} \end{cases} \qquad (9)$$

Figures 8 and 9 represent the morphological variations of the obtained dendrites versus the applied duty cycle **D** and pulse frequency f, respectively, and their tortuosity τ has been quantified in Figure 10, which is consistent with the experimental trends in Figures 6a and 6b.
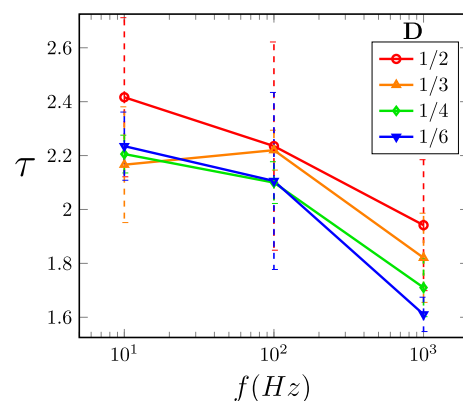

Figure 10. Simulation values for tortuosity τ versus frequency f at different duty cycles **D**.

4. RESULTS AND DISCUSSION

As shown in eq 9, during the pulse period t_{ON}, both diffusion (MSD) and electromigration (EMD) displacements are in action, whereas, during the rest period t_{OFF}, the diffusion (MSD) is the sole driver for ionic motion. Mechanism-wise, the diffusion moves the ions from regions of higher concentration to regions of lower concentration $(-\nabla C)$, which has a tendency to form a uniform ionic distribution. However, the electromigration EMD has a propensity to move the ions in the direction of the electric field from higher electric potential to lower electric potential $(-\nabla V)$. As shown in Figure 7, the tip of the dendrite generates enormous electric fields (blue vectors), because of its curvature and closer proximity to the counter electrode and attracts a larger portion of the upcoming ions. Therefore, the efficacy of pulse charging is to supply a subsequent rest period t_{OFF} for ions to escape away from the dendritic tips by means of diffusion. This moves the growing tendency from fast-growing tips to the slow-growing pores, ending up in a flatter morphology.[52]

From eqs 1 and 2, imposing various Duty cycle D and frequency f values in fact determines the time span for occurrence of electromigration (EMD) and diffusion (MSD) displacements. Elaborating further on the pulse t_{ON} and rest t_{OFF} periods, we get

$$\frac{\partial \mathbf{D}}{\partial t_{ON}} = \frac{t_{OFF}}{(t_{ON} + t_{OFF})^2} > 0$$

which means that the change in the duty cycle $\mathbf{D}$ and pulse period t_{ON} have the same trend. On the other hand, $\mathbf{D}\downarrow = t_{ON}/(t_{ON} + t_{OFF}\uparrow)$, which means the opposite trend between duty cycle and rest period t_{OFF}. In addition, from eq 1, it is obvious that the increase in both t_{ON} and t_{OFF} reduces the frequency f. To summarize:

$$t_{ON} \downarrow \; \Rightarrow \; \mathbf{D} \downarrow, f\uparrow$$

and:

$$t_{OFF} \uparrow \; \Rightarrow \; \mathbf{D} \downarrow, f\downarrow$$

which means that reducing the duty cycle and increasing the frequency should be beneficial for suppressing the fast-growing dendrites. This is in agreement with the trends observed in Figures 6b and 6a, both in terms of the interface tortuosity τ and average dendrite height $\overline{y}$. Moreover, in Figure 6a, the DC charging, which corresponds to $\mathbf{D} = 1$, shows the largest propensity for the dendritic development.

However, there is a limit where the aforementioned parameters remains effective. The pulse period t_{ON} should ultimately be enough for the ions to charge of the double layer and reach the reaction sites for reduction.[65] Therefore, increasing the pulse frequency beyond a certain limit will not noticeably control the dendritic growth.[55] In fact, the range of duty cycle is selected based on the dynamics of the double layer. For example, the maximum value of the duty cycle is found to be $\mathbf{D}_{max} := 1/2$,[54,53] based on the comparison of the reach of the ionic displacements during the pulse t_{ON} and rest t_{OFF} periods, and its minimum value has been experimentally chosen when there is no noticeable difference in the further reduction of the duty cycle $\mathbf{D}$, which is given as $\mathbf{D}_{min} = 1/6$ in the experiments. In other words, the duty cycle $\mathbf{D}$ has been reduced until the following threshold was met for obtaining $\mathbf{D}_{min}$:

$$\frac{\delta \overline{y}}{\delta \mathbf{D}} < 0.1$$

The obtained value for $\mathbf{D}_{min}$ has a close correlation with the previous finding of $\mathbf{D}_{min} = 1/4$ for another setup and cell composition.[52] In addition, the range of the chosen frequency f should encompass the time-scale t_{EXP} for the relaxation of the Debye screening length λ_D, which could be approximated as the geometric mean of the local scale λ_D and the global domain scale of l as[60]

$$t_{EXP} = \frac{\lambda_D l_{EXP}}{D_{EXP}} = 7.7 \text{ ms} \approx 10^{-3} \text{ s}$$

where λ_D is the Debye screening length representing the significance of the electrostatic effect from the charge carrier (eq 4), and D_{EXP} is the diffusivity of Cu^{2+} ions.[61] Since $t_{EXP} \approx 10^{-3}$ s, hence, one expects the upper limit for frequency to be $f_{max} \approx 10^3$ Hz. Imposing duty cycles reduce this value further, and in the range of $D \in [1/6, 1/2]$, one gets $f \in [65, 108]$ Hz. To confidently cover this range, we chose the broader span of $f \in [1, 1000]$ Hz in the experiments.

From Figure 5, it has been observed that the grain sizes have been reduced when imposing higher frequencies. The underlying reason is not allowing the surrounding diffusion layer to grow larger by continuously distorting it during the high frequency/low duty cycle charging. As a result, the particles gain more ordered geometries for lower frequencies/higher duty cycles.

Here, note that, in the experiments, the 3D growth on the electrode surface is captured as a two-dimensional (2D) image, and the aforementioned results are based on the 2D analysis. Therefore, the inhomogeneity in the third direction is not captured for tortuosity measurements, such as a smaller dendrite growing behind a larger one. From another angle, two superimposed similar dendritic structures are likely to contribute one value of tortuosity in that particular frame. As a result, we followed the trend of the tortuosity instead of the exact values.

Needless to mention, since the underlying mechanisms of the dendritic growth from electrodeposition is highly material-dependent,[21,66] the quantitative conclusions from our study are valid for copper. However, the similarity of the trends between lithium and copper strengthens the hypothesis of the efficacy of the pulse charging on the dendritic compression for the larger span of the metallic elements.

5. CONCLUSION

In this paper, we have explained the compression in the dendritic evolution by means of two distinct parameters of duty cycle and frequency in pulse charging. We have shown that the dendrites could shrink by as much as a factor of ∼6 by increasing the pulse frequency f, as well as by a factor of ∼20 by varying the pulse duty cycle $\mathbf{D}$. Establishing an equivalent computationally affordable simulation framework based on coarse-grained modeling, we have shown that the tortuosity of the growing interface has been reduced to 25% and 40% by reducing the duty cycle $\mathbf{D}$ and increasing the frequency f. Moreover, the role of the investigated parameters have been translated versus the pulse t_{ON} and rest t_{OFF} periods, respectively, and their individual role has been analyzed. Finally, the limits of the pulse duty cycle and frequency have been investigated for the efficacy of pulse charging, where the former is related to the relaxation period for the concentration

gradient in the boundary of the electrodeposits, and the latter has been correlated the sufficiency of time for charging the double layer. The obtained characteristic trends are useful for the designing the space of parameters for pulse-charging, particularly for the dendrite-prone systems.

■ ASSOCIATED CONTENT

Ⓢ Supporting Information

The Supporting Information is available free of charge at https://pubs.acs.org/doi/10.1021/acs.jpcc.2c08066.

> Real-time side-by-side video of the dendrite growth for the two duty cycles of $D = \{1/2, 1/4\}$ and the identical frequency of $f = 100$ Hz (MP4)

> Real-time side-by-side videos of the dendrite growth for the two frequencies of $f = \{1,1000\}$ Hz and the identical duty cycle of $D = 1/2$ (MP4)

■ AUTHOR INFORMATION

Corresponding Authors

Asghar Aryanfar — *American University of Beirut, Riad El-Solh, Beirut 1107 2020, Lebanon; Bahçeşehir University, Beşiktaş, Istanbul 34353, Turkey;* ◉ orcid.org/0000-0002-8890-077X; Email: aryanfar@caltech.edu

Sunando DasGupta — *Indian Institute of Technology, Kharagpur, West Bengal 721302, India;* ◉ orcid.org/0000-0002-6365-5077; Email: sunando@che.iikgp.ac.in

Authors

Trina Dhara — *Indian Institute of Technology, Kharagpur, West Bengal 721302, India*

Asmita Ghosh — *Indian Institute of Technology, Kharagpur, West Bengal 721302, India*

Udita Ghosh — *Indian Institute of Technology (BHU), Varanasi, Uttar Pradesh 221005, India*

Partha Mukherjee — *Purdue University, West Lafayette, Indiana 47907, United States*

Complete contact information is available at:
https://pubs.acs.org/10.1021/acs.jpcc.2c08066

Author Contributions

[∇]T.D. and A.A. contributed equally as the first author.

Notes

The authors declare no competing financial interest.

■ REFERENCES

(1) Marom, R.; Amalraj, S. F.; Leifer, N.; Jacob, D.; Aurbach, D. A review of advanced and practical lithium battery materials. *J. Mater. Chem.* **2011**, *21*, 9938−9954.

(2) Goodenough, J. B.; Park, K.-S. The Li-ion rechargeable battery: a perspective. *J. Am. Chem. Soc.* **2013**, *135*, 1167−1176.

(3) Rugolo, J.; Aziz, M. J. Electricity storage for intermittent renewable sources. *Energy Environ. Sci.* **2012**, *5*, 7151−7160.

(4) Dunn, B.; Kamath, H.; Tarascon, J.-M. Electrical energy storage for the grid: a battery of choices. *Science* **2011**, *334*, 928−935.

(5) Cheng, X.-B.; Zhang, R.; Zhao, C.-Z.; Zhang, Q. Toward safe lithium metal anode in rechargeable batteries: a review. *Chem. Rev.* **2017**, *117*, 10403−10473.

(6) Xu, W.; Wang, J. L.; Ding, F.; Chen, X. L.; Nasybulin, E.; Zhang, Y. H.; Zhang, J. G. Lithium metal anodes for rechargeable batteries. *Energy Environ. Sci.* **2014**, *7*, 513−537.

(7) Tarascon, J. M.; Armand, M. Issues and challenges facing rechargeable lithium batteries. *Nature* **2001**, *414*, 359−367.

(8) Shalf, J. The future of computing beyond Moores law. *Philosophical Transactions of the Royal Society A* **2020**, *378*, 20190061.

(9) Brock, D. C.; Moore, G. E. *Understanding Moore's law: four decades of innovation*; Chemical Heritage Foundation, 2006.

(10) Li, Z.; Huang, J.; Yann Liaw, B.; Metzler, V.; Zhang, J. A review of lithium deposition in lithium-ion and lithium metal secondary batteries. *J. Power Sources* **2014**, *254*, 168−182.

(11) Armand, M.; Tarascon, J. M. Building better batteries. *Nature* **2008**, *451*, 652−657.

(12) Xu, H.; Han, C.; Li, W.; Li, H.; Qiu, X. Quantification of lithium dendrite and solid electrolyte interphase (SEI) in lithium-ion batteries. *J. Power Sources* **2022**, *529*, 231219.

(13) Tewari, D.; Rangarajan, S. P.; Balbuena, P. B.; Barsukov, Y.; Mukherjee, P. P. Mesoscale Anatomy of Dead Lithium Formation. *J. Phys. Chem. C* **2020**, *124* 65026511

(14) Aryanfar, A.; Cheng, T.; Goddard, W. A. Bulk Properties of Amorphous Lithium Dendrites. *ECS Trans.* **2017**, *80*, 365−370.

(15) Xu, K. Nonaqueous liquid electrolytes for lithium-based rechargeable batteries. *Chemical Reviews-Columbus* **2004**, *104*, 4303−4418.

(16) Davidson, R.; Verma, A.; Santos, D.; Hao, F.; Fincher, C.; Xiang, S.; Van Buskirk, J.; Xie, K.; Pharr, M.; Mukherjee, P. P.; Banerjee, S. others Formation of magnesium dendrites during electrodeposition. *ACS Energy Letters* **2019**, *4*, 375−376.

(17) Slater, M. D.; Kim, D.; Lee, E.; Johnson, C. S. Sodium-ion batteries. *Adv. Funct. Mater.* **2013**, *23*, 947−958.

(18) Lee, B.; Paek, E.; Mitlin, D.; Lee, S. W. Sodium metal anodes: emerging solutions to dendrite growth. *Chem. Rev.* **2019**, *119*, 5416−5460.

(19) Zheng, J.; Bock, D. C.; Tang, T.; Zhao, Q.; Yin, J.; Tallman, K. R.; Wheeler, G.; Liu, X.; Deng, Y.; Jin, S.; et al. Regulating electrodeposition morphology in high-capacity aluminium and zinc battery anodes using interfacial metal−substrate bonding. *Nature Energy* **2021**, *6*, 398−406.

(20) Pei, P.; Wang, K.; Ma, Z. Technologies for extending zinc air batterys cyclelife: A review. *Applied Energy* **2014**, *128*, 315−324.

(21) Aryanfar, A.; Medlej, S.; Goddard, W. A., III Morphometry of Dendritic Materials in Rechargeable Batteries. *J. Power Sources* **2021**, *481*, 228914.

(22) Ren, Y.; Shen, Y.; Lin, Y.; Nan, C.-W. Direct observation of lithium dendrites inside garnet-type lithium-ion solid electrolyte. *Electrochem. Commun.* **2015**, *57*, 27−30.

(23) Orsini, F; Du Pasquier, A; Beaudoin, B; Tarascon, J.M; Trentin, M; Langenhuizen, N; De Beer, E; Notten, P In Situ Scanning Electron Microscopy (SEM) observation of interfaces with plastic lithium batteries. *J. Power Sources* **1998**, *76*, 19−29.

(24) Schweikert, N.; Hofmann, A.; Schulz, M.; Scheuermann, M.; Boles, S. T.; Hanemann, T.; Hahn, H.; Indris, S. Suppressed lithium dendrite growth in lithium batteries using ionic liquid electrolytes: Investigation by electrochemical impedance spectroscopy, scanning electron microscopy, and in situ Li-7 nuclear magnetic resonance spectroscopy. *J. Power Sources* **2013**, *228*, 237−243.

(25) Younesi, R.; Veith, G. M.; Johansson, P.; Edström, K.; Vegge, T. Lithium Salts for Advanced Lithium Batteries: Li-metal, Li-O 2, and Li-S. *Energy Environ. Sci.* **2015**, *8*, 1905−1922.

(26) Nielsen, C. P.; Bruus, H. Morphological instability during steady electrodeposition at overlimiting currents. *Phys. Rev. E* **2015**, *92*, 052310.

(27) Natsiavas, P.; Weinberg, K.; Rosato, D.; Ortiz, M. Effect of prestress on the stability of electrode−electrolyte interfaces during

charging in lithium batteries. *Journal of the Mechanics and Physics of Solids* **2016**, *95*, 92−111.

(28) Ishikawa, M.; Machino, S.-i.; Morita, M. Electrochemical control of a Li metal anode interface: improvement of Li cyclability by inorganic additives compatible with electrolytes. *J. Electroanal. Chem.* **1999**, *473*, 279−284.

(29) Aryanfar, A.; Brooks, D. J.; Colussi, A. J.; Merinov, B. V.; Goddard, W. A., III; Hoffmann, M. R. Thermal relaxation of lithium dendrites. *Phys. Chem. Chem. Phys.* **2015**, *17*, 8000−8005.

(30) Aryanfar, A.; Cheng, T.; Colussi, A. J.; Merinov, B. V.; Goddard, W. A., III; Hoffmann, M. R. Annealing kinetics of electrodeposited lithium dendrites. *J. Chem. Phys.* **2015**, *143*, 134701.

(31) Ding, F.; Xu, W.; Graff, G. L.; Zhang, J.; Sushko, M. L.; Chen, X.; Shao, Y.; Engelhard, M. H.; Nie, Z.; Xiao, J.; et al. Dendrite-free lithium deposition via self-healing electrostatic shield mechanism. *J. Am. Chem. Soc.* **2013**, *135*, 4450−4456.

(32) Chen, M.; Shao, M.; Jin, J.; Cui, L.; Tu, H.; Fu, X. Configurational and structural design of separators toward shuttling-free and dendrite-free lithium-sulfur batteries: A review. *Energy Storage Materials* **2022**,.47629

(33) Zhou, W.; Chen, M.; Tian, Q.; Chen, J.; Xu, X.; Wong, C.-P. Cotton-derived cellulose film as a dendrite-inhibiting separator to stabilize the zinc metal anode of aqueous zinc ion batteries. *Energy Storage Materials* **2022**, *44*, 57−65.

(34) Choudhury, S.; Vu, D.; Warren, A.; Tikekar, M. D.; Tu, Z.; Archer, L. A. Confining electrodeposition of metals in structured electrolytes. *Proc. Natl. Acad. Sci. U. S. A.* **2018**, *115*, 6620−6625.

(35) Bhange, D. S.; Anang, D. A.; Ali, G.; Park, J.-H.; Kim, J.-Y.; Bae, J.-H.; Yoon, W. Y.; Chung, K. Y.; Nam, K.-W. NaFeSnO4: Tunnel structured anode material for rechargeable sodium-ion batteries. *Electrochem. Commun.* **2020**, *121*, 106873.

(36) Ye, X.; Xiong, W.; Huang, T.; Li, X.; Lei, Y.; Li, Y.; Ren, X.; Liang, J.; Ouyang, X.; Zhang, Q.; Liu, J. A blended gel polymer electrolyte for dendrite-free lithium metal batteries. *Appl. Surf. Sci.* **2021**, *569*, 150899.

(37) Li, Q.; Zhu, S.; Lu, Y. 3D porous Cu current collector/Li-metal composite anode for stable lithium-metal batteries. *Adv. Funct. Mater.* **2017**, *27*, 1606422.

(38) Liu, Y. Overview of the Recent Progress of Suppressing the Dendritic Growth on Lithium Metal Anode for Rechargeable Batteries. *Journal of Physics: Conference Series.* **2022**; p 012060.

(39) Chazalviel, J. N. Electrochemical Aspects of the Generation of Ramified Metallic Electrodeposits. *Phys. Rev. A* **1990**, *42*, 7355−7367.

(40) Monroe, C.; Newman, J. Dendrite growth in lithium/polymer systems - A propagation model for liquid electrolytes under galvanostatic conditions. *J. Electrochem. Soc.* **2003**, *150*, A1377−A1384.

(41) Witten, T. A.; Sander, L. M. Diffusion-limited aggregation. *Phys. Rev. B* **1983**, *27*, 5686.

(42) Fleury, V.; Rosso, M.; Chazalviel, J. N. Geometrical Aspect of Electrodeposition - the Hecker Effect. *Phys. Rev. A* **1991**, *43*, 6908−6916.

(43) Fleury, V.; Chazalviel, J.-N.; Rosso, M.; Sapoval, B. The role of the anions in the growth speed of fractal electrodeposits. *J. Electroanal. Chem. Interfacial Electrochem.* **1990**, *290*, 249−255.

(44) Fleury, V.; Chazalviel, J.-N.; Rosso, M. Coupling of drift, diffusion, and electroconvection, in the vicinity of growing electrodeposits. *Phys. Rev. E* **1993**, *48*, 1279.

(45) Fleury, V. Branched fractal patterns in non-equilibrium electrochemical deposition from oscillatory nucleation and growth. *Nature* **1997**, *390*, 145−148.

(46) Mayers, M. Z.; Kaminski, J. W.; Miller, T. F., III Suppression of Dendrite Formation via Pulse Charging in Rechargeable Lithium Metal Batteries. *J. Phys. Chem. C* **2012**, *116*, 26214−26221.

(47) Garcia, G.; Ventosa, E.; Schuhmann, W. Complete prevention of dendrite formation in Zn metal anodes by means of pulsed charging protocols. *ACS Appl. Mater. Interfaces* **2017**, *9*, 18691−18698.

(48) García, G.; Dieckhöfer, S.; Schuhmann, W.; Ventosa, E. Exceeding 6500 cycles for LiFePO 4/Li metal batteries through understanding pulsed charging protocols. *Journal of Materials Chemistry A* **2018**, *6*, 4746−4751.

(49) Yang, H.; Fey, E. O.; Trimm, B. D.; Dimitrov, N.; Whittingham, M. S. Effects of pulse plating on lithium electrodeposition, morphology and cycling efficiency. *J. Power Sources* **2014**, *272*, 900−908.

(50) Aryanfar, A.; Ghamlouche, Y.; Goddard, W. A. Optimization of charge curve for the extreme inhibition of growing microstructures during electrodeposition. *MRS Bull.* **2022**, *47*, 665.

(51) Aryanfar, A.; Ghamlouche, Y.; Goddard, W. A., III Pulse Reverse Protocol for efficient suppression of dendritic microstructures in rechargeable batteries. *Electrochim. Acta* **2021**, *367*, 137469.

(52) Aryanfar, A.; Brooks, D.; Merinov, B. V.; Goddard, W. A., III; Colussi, A. J.; Hoffmann, M. R. Dynamics of Lithium Dendrite Growth and Inhibition: Pulse Charging Experiments and Monte Carlo Calculations. *J. Phys. Chem. Lett.* **2014**, *5*, 1721−1726.

(53) Aryanfar, A.; Ghamlouche, Y.; Goddard, W. A., III Real-time control of dendritic propagation in rechargeable batteries using adaptive pulse relaxation. *J. Chem. Phys.* **2021**, *154*, 194702.

(54) Aryanfar, A.; Hoffmann, M. R.; Goddard, W. A., III Finite-pulse waves for efficient suppression of evolving mesoscale dendrites in rechargeable batteries. *Phys. Rev. E* **2019**, *100*, 042801.

(55) Dhara, T.; Ghosh, U. U.; Ghosh, A.; Vishnugopi, B. S.; Mukherjee, P. P.; DasGupta, S. Mechanistic Underpinnings of Morphology Transition in Electrodeposition under the Application of Pulsatile Potential. *Langmuir* **2022**, *38*, 4879−4886.

(56) Collins, T. J. ImageJ for microscopy. *Biotechniques* **2007**, *43*, S25−S30.

(57) Otsu, N. A threshold selection method from gray-level histograms. *IEEE transactions on systems, man, and cybernetics* **1979**, *9* (1), 62−66.

(58) Philibert, J. One and a half century of diffusion: Fick, Einstein, before and beyond. *Diffusion Fundamentals* **2006**, *4*, 1−19.

(59) Slater, J. C. Atomic radii in crystals. *J. Chem. Phys.* **1964**, *41*, 3199−3204.

(60) Bazant, M. Z.; Thornton, K.; Ajdari, A. Diffuse-charge dynamics in electrochemical systems. *Phys. Rev. E* **2004**, *70*. DOI: 10.1103/PhysRevE.70.021506

(61) Noulty, R. A.; Leaist, D. G. Diffusion in aqueous copper sulfate and copper sulfate-sulfuric acid solutions. *Journal of solution chemistry* **1987**, *16*, 813−825.

(62) Physics, C. O. F.; Nist, C.; June, S. P. 2018 CODATA Recommended Values of the Fundamental Constants of Physics and Chemistry. *Natl. Inst. Stand. Technol.* **2019**, *959*, 1−2.

(63) Malmberg, C.; Maryott, A. Dielectric constant of water from 0 to 100 C. *J. Res. Natl. Bur. Stand.* **1956**, *56*, 1−8.

(64) Newell, D. B.; Tiesinga, E. The international system of units (SI). *NIST Special Publication* **2019**, *330*, 1−138.

(65) Puippe, J. C.; Ibl, N. Influence of charge and discharge of electric double layer in pulse plating. *J. Appl. Electrochem.* **1980**, *10*, 775−784.

(66) Bai, P.; Li, J.; Brushett, F. R.; Bazant, M. Z. Transition of lithium growth mechanisms in liquid electrolytes. *Energy Environ. Sci.* **2016**, *9*, 3221−3229.

■ NOTE ADDED AFTER ASAP PUBLICATION

This paper published February 17, 2023 with a production error in Table 1. The error was corrected and the revised paper was reposted on February 22, 2023.